J. Physical Chemistry C

Tuning the Magnetic Moment of FePc/Ag(110) Monolayer Phases through Oxygen Dosing

E. Bartolomé[1], J. Bartolomé[2], F. Sedona[3], J. Lobo-Checa[2], D. Forrer[3], J. Herrero-Albillos[4], M. Piantek[5], J. Herrero-Martín[6], D. Betto[7], E. Velez-Fort[7], L.M. García[2], M. Panighel[8], A. Mugarza[9,10], M. Sambi[3], F. Bartolomé[2]

[1] *Escola Universitària Salesiana de Sarrià (EUSS), Passeig Sant Joan Bosco 74, 08017 Barcelona, Spain*
[2] *Instituto de Ciencia de Materiales de Aragón and Departamento de Física de la Materia Condensada, CSIC-Universidad de Zaragoza, Pedro Cerbuna 12, 50009 Zaragoza, Spain.*
[3] *CNR-ICMATE, Department of Chemical Sciences, University of Padova, via Marzolo 1, 35131 Padova, Italy*
[4] *Centro Universitario de la Defensa. Academia General Militar, Zaragoza, Spain*
[5] *Instituto de Nanociencia de Aragón, Universidad de Zaragoza, Zaragoza, Spain*
[6] *ALBA synchrotron, Bellaterra, 08193-Barcelona, Spain*
[7] *ESRF-The European Synchrotron Radiation Facility, Grenoble, France*
[8] *CNR-IOM Laboratorio TASC, S.S. 14 km 163, Basovizza, I-34149 Trieste, Italy*
[9] *Catalan Institute of Nanoscience and Nanotechnology (ICN2), CSIC and Barcelona Institute of Science and Technology, Campus UAB, Bellaterra, 08193 Barcelona, Spain*
[10] *ICREA - Institució Catalana de Recerca i Estudis Avançats, 08010 Barcelona, Spain*

Received: xx, 2020; Revised Manuscript Received: xx, 2020

Iron-phtalocyanines (FePc) adsorbed onto a Ag(110) substrate self-assemble into different monolayer phases going from rectangular to different oblique phases, with increasing molecular density. We have investigated the oxygen uptake capability of the different phases and their associated magneto-structural changes. Our study combines scanning tunneling microscopy and spectroscopy (STM/STS), X-ray magnetic circular dichroism (XMCD), and density functional theory (DFT) calculations. STM measurements reveal that the oxidation reaction of the FePc/Ag(110) generally involves a displacement and a rotation of the molecules, which affects the electronic state of the Fe centers. The oxygen intercalation between FePc and the substrate is greatly obstructed by the steric hindrance in the high-density phases, to the point that a fraction of oblique phase molecules cannot change their position after oxydizing. Depending on the oxidation state and adsoption geometry, the STS spectra evidence clear differences in the Fe local density of states, which are mirrored in the XAS and XMCD experiments. Particularly, XMCD spectra of the oxidized phases reflect the distribution of FePc species (non-oxygenated, oxygenated-rotated and oxygenated-unrotated) in the different cases. Sum rule analysis yields the effective spin (m_s^{eff}) and orbital (m_L) magnetic moments of Fe in the different FePc species. Upon oxidation, the magnetic moment of FePc molecules increases about an order of magnitude, reaching m_{TOT}~2.2 μ_B per Fe atom.

1. INTRODUCTION

Molecular overlayers on crystalline substrates have a broad field of application in catalysis, sensing, molecular electronics, light-to-energy conversion, etc. In particular, bio-inspired oxygen-binding metalated macrocycles, such as iron-phtalocyanines (FePc), are investigated as viable substitutes for precious metals in catalysis of the Oxygen Reduction Reaction in low-temperature fuel cells.

Recently, the spontaneous assembly and the electronic and magnetic properties of FePc have been studied on a variety of substrates: Au(111)[1–3], Au(001)[4], Au(100)[5], TiO_2(110)[6], InAs(100)[7], InSb(100)[7], Cu(110)[8], NaCl/Cu(111)[9], Ag(111)[10,11], graphite[12] and grahene/Cu(111), Ni(111)[13]. In particular, FePc/Ag(110) has been intensively investigated to shed light into the self-assembly, interaction mechanisms, structural transformations upon thermal treatments, and its capacity to accommodate small molecules like O_2.

The properties of FePc sublimated onto Ag(110) were first investigated by Palmgren *et al*.[14] by low energy electron diffraction (LEED). Casarin *et al*.[15] reported coverage-dependent structural and self-assembly properties of FePc based on STM and DFT simulations. They found that in the monolayer regime, FePc molecules lie flat on the Ag(110) surface. At molecular densities below 0.449 molecules per nm^2, a mixture of two structurally distinct, equally dense phases coexist, namely c(10x4) = R1, and p(10x4) = R2 phases. Both phases stabilize upon annealing in UHV between 410 and 520 K. The R1 phase has a centered rectangular unit cell, as shown in Fig. 1. In this phase, Fe centers ocupy sites on-top of a silver atom (OT sites) and all the molecules are oriented alike, with the molecular axis bisecting the phenyl rings forming a 45º angle with the substrate [1$\bar{1}$0] direction (OT-45 positions, see Fig. 2a). The R2 phase is formed by the ordered and alternated sequence of singly oriented rows parallel to the [001] direction of the Ag substrate (see Fig. 1). In this phase, Fe centers occupy short-bridge sites between two silver atoms (SB sites), and the FePc phenyl rings are rotatet 30º (either clockwise or anticlockwise) with respect to the substrate [1$\bar{1}$0] direction (SB-30 positions, see Fig. 2b).

At higher molecular density (≈0.449 molecules per nm^2) the thermal treatment stabilizes an oblique phase (OB1), as reported by Sedona *et al*.[16]. The molecular adsorption site and possible local orientations in the OB1 phase with respect to the substrate are those described for the R2 phase: in the OB1 phase the Fe centers occupy SB sites and all of them have the same orientation, either +30º or -30º within the same ordered domain. Cai *et al*.[17] did observe two additional "oblique" arrangements of FePc on Ag(110), which we have not found reproducibly as stable phases.

Interestingly, low-density R1 and R2 phases have been shown to be catalytically active[16]. Upon oxidation of these two phases, oxygen atoms intercalate between the FePc and the substrate, forming the FePc-(η^2-O_2)-Ag coordination complex. The oxygen uptake in R2 phase involves shifting and rotating the molecules

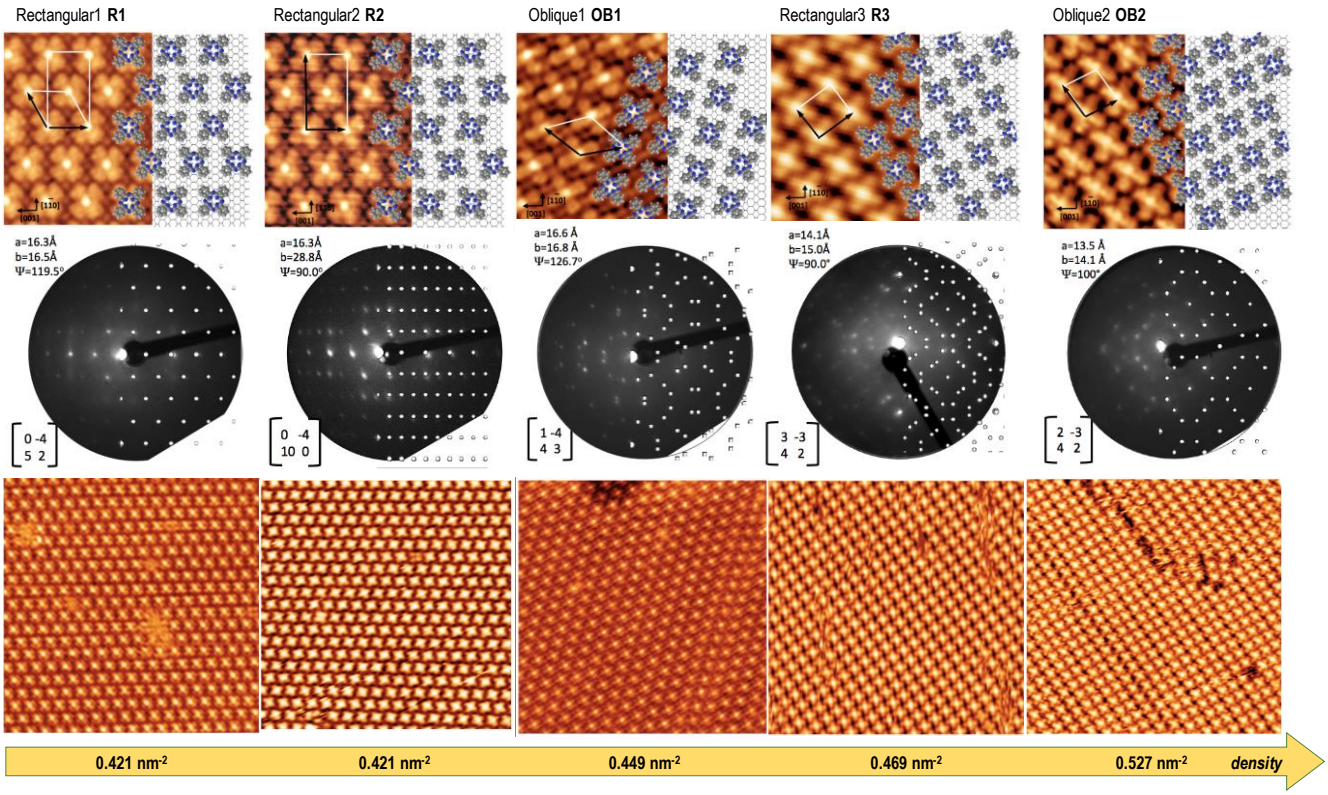

Figure 1. FePc/Ag(110) sub-ML phases with increasing molecular density (from left to right). Each column identifies a phase containing an STM image acquired at room temperature, the unit cell model, the matrix notation and the LEED pattern with the corresponding simulation of the phase. STM imaging parameters for the top (75x55 Å^2) images: R1 (0.4 V, 0.3 nA), R2 (0.4 V, 0.7 nA), OB1 (3.2 V, 9.0 nA), R3 (-0.9 V, 0.8 nA), OB2 (0.6 V, 0.4 nA). LEED parameters: R1(28 eV), R2 (30 eV), OB1 (28 eV), R3 (35 eV), OB2 (30 eV).

from its original SB-30 to an OX(OT-45) position, and adsorbing two oxygen atoms at the neighboring SB sites, as shown in Fig. 2c (in the pristine R1 phase the FePc molecule is already positioned on OT-45). Remarkably, this process decouples the molecular electronic states from the metal surface resulting in a concomitant increase of one order of magnitude of the Fe magnetic moment (from $m_T \approx 0.26$ μ_B to $m_{TOT} \approx 2.1$ μ_B), as demonstrated by XMCD.

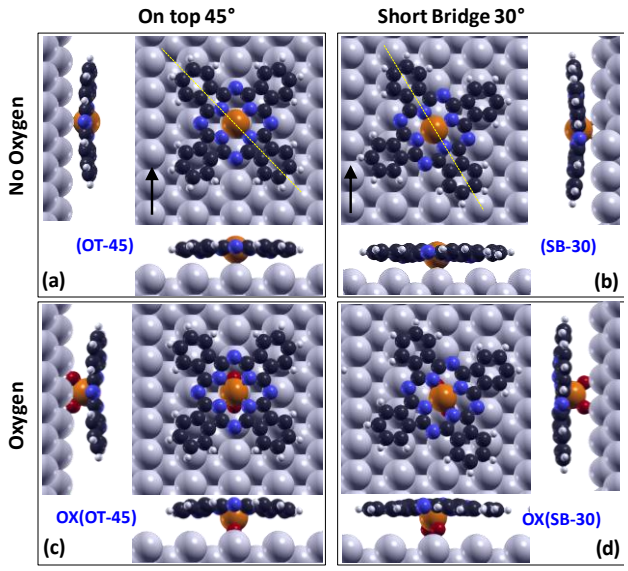

Figure 2. Different geometries of as deposited and oxidized molecules in FePc/Ag(110) phases: top and lateral views.

Notably, the molecular arrangement and the Fe magnetic moment is reversible upon oxidation-annealing cycles[18].

However, the oxidation of high-density FePc phases on Ag(110) is still unreported. It is known that in the related case of high-density FePc on Ag(100)[19], oxygen is adsorbed (as di- and mono-oxygen) on-top of the Fe centers instead of being intercalated between the molecular layer and the substrate[20]. In this case, the FePc reactivity to oxidation seems to be mediated by the presence of Ag adatoms between the molecules, therefore involving a completely different reaction mechanism with respect to Ag(110). A temptative explanation for this difference assumes, on one hand, that Ag(100) is atomically "flat" compared to the corrugated Ag(110), which hinders the dissociation and transport of oxygen underneath the FePc molecules, and on the other hand that on Ag(110) there is no evidence of the presence of Ag adatomns in-between the FePc molecules.

In this paper we report the formation of new high-density FePc/Ag(110) phases in the sub-ML to ML regime, which, despite their steric limitations, still present catalytic activity, at variance with the saturated Fe/Ag(100) monolayer. The oxygen intercalation capability and associated magnetization changes of these high-density phases are reported by correlating high-resolution STM images, STS spectra, XMCD measurements and DFT calculations, and systematically compared with the analogous results obtained on the low-density phases, thereby obtaining a more detailed description of this complex and intringuing system.

2. METHODS

Samples. FePc molecules were evaporated on a Ag(110) single crystal substrate in several ultrahigh vacuum (UHV) chambers (base pressures in the low 10^{-10} mbar range), containing equipment

for sample sputtering, thermal annealing, FePc deposition, and connected to the XAS & XMCD experimental chamber. The Ag(110) single-crystal was cleaned by repeated cycles of 1keV Ar^+ sputtering and annealing at 550ºC (10 min). The surface quality and order was monitored by LEED.

A few mg of FePc (Alfa Aesar GmbH, 95% purity) were loaded into a pyrolytic boron nitride (PBN) crucible connected to the preparation chamber. The FePc sample was carefully degassed while monitoring the UHV base pressure. The crucible temperature was raised to 540 K in approximately 30 h, held at this temperature for 25 h and increased to 560-570 K for additional 6 h. Depositions were performed with the crucible temperature at 550 K. The Ag substrate was held at room temperature (RT) during molecular deposition. Different sub-ML phases of FePc/Ag(110) were prepared, and the structure controlled *in situ* by LEED.

The oxidation of the FePc deposited on the Ag substrate was achieved by exposing the sample surface to an oxygen pressure *P*, for a time *t* (*P* x *t* Langmuir) in the closed chamber at room temperature. The exposures for the samples used in this paper are collected in Table S1.

STM. The structural evolution of FePc phases up to the full ML with the oxygen dosing was monitored by Scanning Tunnelling Microscopy (STM). The experiments were performed using two different instruments: a room-temperature setup (Omicron VT-STM) at the University of Padova, and a low temperature equipment (Omicron LT-STM) operated at 4.6 K at the *Laboratorio de Microscopías Avanzadas* (LMA, Zaragoza).

STS. Differential conductance (d*I*/d*V*) curves at the Fe centres were obtained using the Omicron LT-STM at 4.6 K in two different operating modes: with open feedback loop at constant tip height (CH) and in constant current (CC) mode. While the CH mode is generally used to measure the local density of states (LDOS) around the Fermi level, we found more convenient to close the feedback-loop (CC mode) for extended voltage ranges in order to avoid structural damage of tip and sample by excessive electric fields and/or electron injection. Here we combined the two modes in order to obtain the spectra over the entire range of interest. For better visualisation, the CC data is multiplied by a constant factor in order to stich the experimental curves. It should be noted, that we refrain from comparing different phases' spectra measured in separate experimental runs since the tip apex termination was found to be altered. Given that the surface was saturated with molecules, we did not have full control over the tip nanostructuring that ultimately influence the d*I*/d*V* spectral lineshape (the observed signal is a convolution of both the sample and tip LDOS).

DFT. DFT+U calculations were performed on FePc adsorbed on Ag(110) before and after the oxygen dosage, using the Quantum-ESPRESSO suite of codes[21]. As we need to deal with two different adsorption configurations, i.e. the SB-30 and rotated OT-45, simulations were run on a p(6x4) rectangular cell, which can allocate both geometries. The PBE[22] exchange-correlation functional was adopted and wavefunctions were expanded on a plane-wave basis set with a cut-off of 27 Ry, while the cut-off on the density was 250 Ry and a 2x2 mesh of k-points was used. The interaction between valence electrons and ion cores was described through ultrasoft pseudopotentials[23]. The Hubbard U was used on the Fe site only and was set to 3.9 eV[24]. STM images were simulated within the Tersoff-Hamann approach[25], while STS curves were compared to the density of states projected on the Fe $3d_{z^2}$ atomic orbital. Atomic charges, magnetizations and holes were computed within a Löwdin approach as in our previous work[18].

XLPA, XAS, XMCD. Soft X-ray absorption and magnetic dichroism experiments at the Fe $L_{2,3}$ and N K edges were carried out at ALBA (BOREAS beamline[26]) and ESRF (ID-32[27,28]) synchrotron radiation facilities. The sample was oriented with the Ag[1$\bar{1}$0] direction perpendicular to the beam plane of incidence. Experiments were performed with the X-ray beam forming an angle of incidence $0 < \gamma < 70^o$ with the normal to the substrate. The detection mode was total electron yield (TEY).

In X-ray linear polarized absorption (XLPA) measurements, the polarization of incident X-ray is denoted as horizontal (H) and vertical (V) for parallel and perpendicular, respectively, to the synchrotron ring plane.

X-ray magnetic circular dichroism (XMCD) spectra were measured at ALBA (BOREAS, *B*=6 T, *T*=3.4 K) and ESRF (ID8, *B*=4 T, *T*=6.0 K) endstations, respectively, to guarantee magnetic saturation. To rule out experimental artifacts and reduce drift phenomena, XMCD was measured by either changing the light helicity or the field direction. To increase statistics, the XMCD spectra were determined from up to 16 XAS spectra with right- and left-handed circular polarizations.

To determine the FePc signal, the background contribution from the Ag substrate has to be carefully subtracted. X-ray absorption spectroscopy (XAS) and XLPA experiments on pristine Ag substrates were performed under the same experimental conditions used for FePc/Ag(110) samples. The background-subtracted XAS and XLPA spectra were subsequently normalized to the atomic continuum signal well above the Fe $L_{2,3}$ absorption edges.

3. RESULTS

3.1 Modification of FePc/Ag(110) phases upon oxidation.

At room temperature, FePc on Ag(110) self-assembles up to the ML in several ordered phases, all of them characterised by flat-lying molecular overlayers. We detect five FePc phases when increasing the surface density, with occupation densities ranging from 0.421 to 0.527 molecules per nm^2. Fig. 1 summarizes these arrangements by showing their STM topography, LEED pattern, structural model and matrix notation with respect to the Ag(110) substrate.

At low densities, the surface is characterised by a mixture of the rectangular R1 and R2 phases, that show the same centred unit cell dimensions. By increasing the FePc density, the oblique OB1 phase is stabilized with 0.449 molecule/nm^2. At even higher densities, two other phases appear (with a unit cell almost squared but slightly distorted): R3 phase, and a new oblique phase OB2. Among the five phases reported in Fig. 1, only in R1 the Fe is found in OT-45 configuration, whereas in all the other phases the Fe is in SB-30 positions. The R3 and OB2 phases often coexist, likely because of their similar structure (see also Fig. S1). Due to this similarity, in the subsequent discussion regarding oxidation they are treated as equivalent ($R3^{OX}$/$OB2^{OX}$).

Fig. 3 shows STM images exhibiting the effect of exposing to oxygen the different phases. Before oxidation (Fig. 3, top panel), the FePc molecules characteristically show a bright central spot corresponding to the Fe atom. Oxygen uptake has the effect of "dimming" this central point (Fig. 3, mid panels). This phenomenon was earlier reported for low-density phases R1/R2. The formation of the FePc-(η_2-O_2)-Ag complex is accompanied by a downward pull of the Fe atom, which is well below the macrocycle plane (as visible in Fig. 2c, 2d side views). The oxidized Fe atoms present also a different electronic configuration, and appear as dark spots in the STM images. The high-resolution STM image Fig. 3g shows the $R1/R2^{OX}$ phase contains a distribution of non-oxidized molecules and oxidized molecules, OX(SB-30), see green box.

We have found that OB1, R3 and OB2 high-density phases are also catalytically active and behave similarly to R1 and R2, as evidenced in the middle and bottom rows of Fig. 3.

Fig. 3i displays a high-resolution STM image of a highly oxygen-dosed phase $R3^{OX}$, where approximately 80% of the

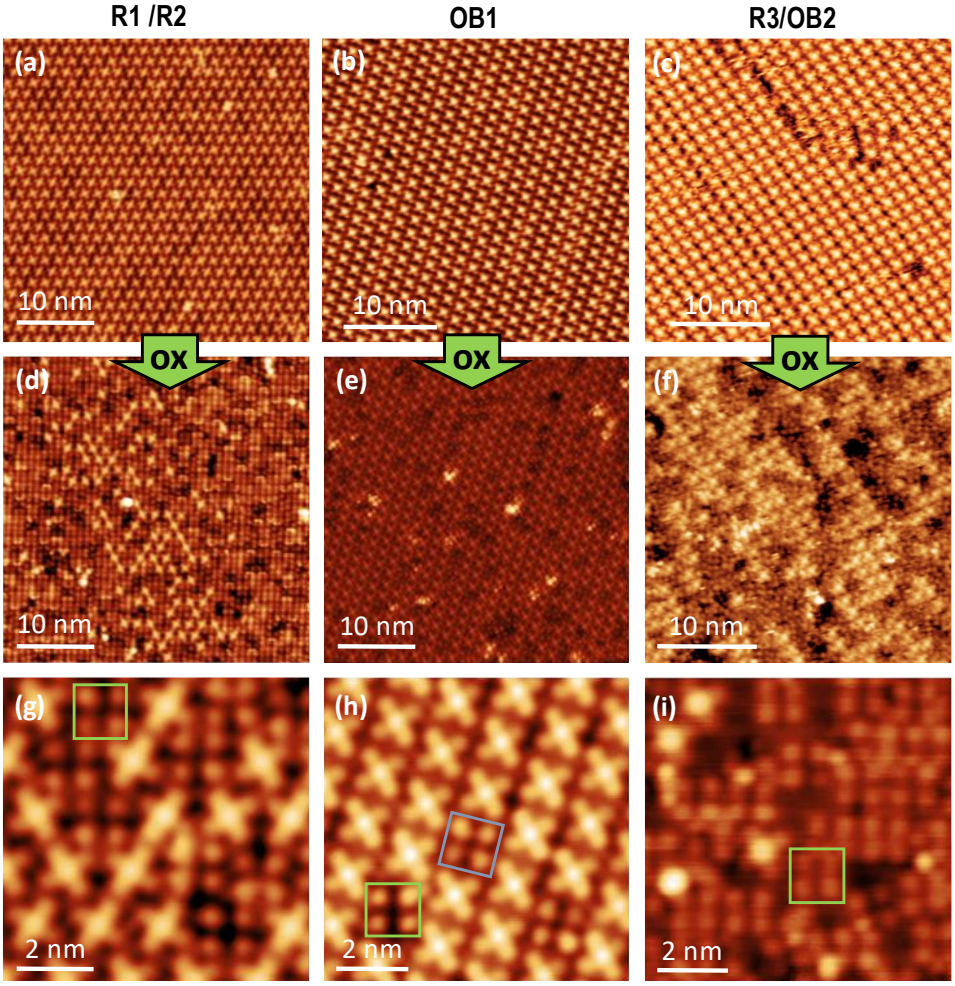

Figure 3. Catalytic activity of the different FePc/Ag(110) phases. *Top panels:* STM images of pristine phases: (a) R1/R2 (V = 0.5 V, I =0.1 nA), (b) OB1 (0.5 V, 0.1 nA), (c) R3/OB2 (-1 V, 2.5 nA); *Middle panels:* images of partially oxidized phases: (d) $R1^{OX}$ /$R2^{OX}$ (0.5 mV, 0.2 nA), (e) $OB1^{OX}$ (0.4 V, 0.1 nA), (f) R3 ^{OX}/$OB2^{OX}$ (-1 V, 5.7 nA). Non-oxidized molecules are recognizable by their bright centers, while oxidized molecules have dark centers; *Bottom panels:* high-resolution STM images of oxidized phases. (g) $R1^{OX}$/$R2^{OX}$ (0.5 V, 0.15 nA), (h) $OB1^{OX}$ (0.5 V, 0.2 nA), (i) $R3^{OX}$ (0.5 V, 0.05 nA). The $R1^{OX}$/$R2^{OX}$ and $R3^{OX}$/$OB2^{OX}$ phases contain a distribution of non-oxidized molecules (SB-30) and oxidized, rotated molecules OX(OT-45). In contrast, the $OB1^{OX}$ phase contains a distribution of non-oxidized FePc at SB-30 and two species of oxidized FePc: OX(OT-45) (green box) and OX(OT-30) (blue box).

molecules were oxidized. In comparison with previously reported oxidized $R1^{OX}$ and $R2^{OX}$, the high-density oxidized $R3^{OX}$ phase shows considerable disorder. Indeed, numerous vacancies appear and occasionally phenyl rings of neighboring oxidized molecules overlap. Fig. S2 (top) shows a zoom into a non-oxidized molecule (SB-30) and an oxidized one, OX(OT-45). The oxidation mechanism in the $R3^{OX}$ phase therefore resembles the one found in $R2^{OX}$ phase, although the increased molecular density strongly distorts the initial arrangement by introducing disorder due to steric hindrance.

In the case of the oblique phase after oxidation ($OB1^{OX}$) shown in Fig. 3h, the system largely maintains its initial arrangement. As extracted from this figure, we can distinguish mainly three FePc species: i) a majority of non-oxidized molecules, which remain at their original SB-30 positions (bright centers); ii) oxidized, rotated molecules in OX(OT-45) positions (green box in Fig. 3h), resembling the oxidized molecules in $R2^{OX}$ and $R3^{OX}$ phases, and iii) oxidized, non-rotated molecules maintaining their original positions, OX(SB-30), blue box in Fig. 3h. This last species had not been previously reported. In Fig. 3i we find 70% of non-oxidized molecules, 22% of OX(SB-30) and 8% of OX(OT-45) oxidized species. It is not surprising that the OB order is preserved by the SB-30 species, while grain boundaries are generated around FePc's shifting into OT-45 sites upon oxidation. It is evident that in the $OB1^{OX}$ phase the FePc molecules struggle to accommodate oxygen underneath, as seen by the STM image of oxidized molecules and their corresponding profiles along the pyrrole rings (Fig. S2, bottom). Even if all non-oxidized molecules for the high-density phases start from SB-30 configuration, the oxidizing activity of this OB phase is significantly lower compared to the R3 and OB2 phases, even when these two present a higher molecular density. Therefore, the local molecular environment might be the key for a higher reaction efficiency, as it can probably control the ultimate molecular degrees of freedom.

3.2 Spectroscopy of molecular species in selected phases.

STS experiments and DFT calculations have been performed to follow the changes upon oxidation in the local density of states of the Fe centers. The square planar symmetry around Fe in the non-oxidized molecules is modified when oxidized, since the Fe is shifted downwards and has 4 N and 2 O atoms as nearest neighbors, with local C2 symmetry[29]. One may expect therefore a strong

change in the electronic states. We assume that the Fe ions are practically unaffected by adjacent molecules, so only three molecular species have to be considered: non-oxidized SB-30, oxidized OX(OT-45) and OX(SB-30). These molecular species can be identified on partially oxidized $R2^{OX}$ and $OB1^{OX}$ samples. Their STS spectra are measured with the tip of the microscope on top of the Fe atoms, either oxidized and non-oxidized. The energy positions of the spectral features are summarized in Table S2.

Fig. 4a shows the STS spectra corresponding to the partially oxidized $R2^{OX}$ low-density phase. The non-oxidized SB-30 molecules are found at SB-30 positions either clockwise or counter-clockwise rotated. They are found to exhibit identical conductance spectra. Their spectrum (red line) exhibits resonances at -1.15 V (a) and -0.32 V (b) below the Fermi level. Weaker features corresponding to unoccupied states can be found above the Fermi level: peak (c) at +0.80 V and an incomplete peak (d) in the proximity of +2 V.

In contrast, the spectrum at the Fe center of the oxidized molecule OX(OT-45) (green line) shows only one dominant feature (e) above the Fermi level at +1.52 V, and another below the Fermi level (a) at -1.14 V.

For the oxidized high-density $OB1^{OX}$ phase (Fig. 4b), we acquired the STS of the three different species. In the case of the pristine (non-oxidized) FePc (red line), despite the different tip LDOS, we find a close resemblance to the R2-phase spectrum, which is expected since in both cases molecules have the Fe centers at SB-30 adsorption sites. In contrast, the oxidized species can correspond either to rotated molecules OX(OT-45), green line, or to unrotated FePc species, OX(SB-30), blue line.

The spectrum of Fe in OX(SB-30) molecules shows a new resonance at -0.80 V, peak (f), absent in the rotated molecule OX(OT-45), but no other peak is found in the occupied PDOS region (note we assign the small features between -0.5 V and the Fermi energy to tip contributions). In the region above the Fermi level, the dominant peaks (e') and (e) are found at +1.58 eV for the OX(SB-30) and at +1.78 eV for OX(OT-45), respectively. Moreover, the spectrum of OX(OT-45), blue line, exhibits a broad resonance (c) close to +1.0 eV. Importantly, these energy differences allow us to spectroscopically distinguish the two oxidized species.

These experimental results can be compared to the PDOS predictions for the different d orbitals, calculated for the three molecular species depicted in Fig. 2. The experimental STS appears to follow closely the d_{z^2} orbital PDOS predictions, as displayed in Fig. 4c, and to be less sensitive to the other calculated orbitals that are shown in Fig. S3. A reason for this orbital selection relates to the instrumental response since the tip is prone to interact predominantly with vertically protruding wavefunctions, which fulfills with the d_{z^2} orbitals geometry.

In the case of the pristine FePc in SB-30 (red line in Fig. 4c), the dominant peak (b) in the occupied region corresponds to the HOMO orbital of the molecule, which energetically agrees well with the experimental spectra observed for the R2 and OB1 phases (Table S2). The occupied peak (a), which is clearly observed in R2 but barely visible in OB1 at a lower energy, is neatly present in the calculation, in good agreement with the experimental result in R2. Above the Fermi level, peaks (c) and (d) can also be correlated with the experiments, albeit these peaks are weak and show slight energy shifts.

Noteworthy is that in the occupied region we find experimentally that the oxidized rotated species OX(OT-45) in the $R2^{OX}$ exhibits the state (a) below the Fermi level, but lack the HOMO peak (b). The absence of this peak in the OX(OT-45) species of both phases could be interpreted as a quench of the HOMO state when the molecules oxidise and rotate. Contrarily, the existence of peak (f) in $OB1^{OX}$ (SB-30) in proximity to (b) suggests a gentle electronic reconfiguration of the HOMO state whenever the oxidized molecules are unable to rotate. In the unoccupied region, both oxidized species experimentally show dominant peaks (e) and (e') close to +1.8 V, which find its match in the calculations even if slight energy deviations are observed.

In essence, the STS main experimental features are well reproduced by our theoretical calculations. Importantly, the HOMO quenching (peak (b)) and concomitant appearance of the dominant unoccupied states ((e) and (e')) evidences a strong reconfiguration of the electronic density of metallic d- states upon oxidation that simply depend on the adsorption position (determined by the molecule rotation) of the individual oxidized molecules. To understand the extent of the electron transfer of the central Fe-ion upon oxygen adsorption we complement our findings by studying these systems using surface averaging XMCD.

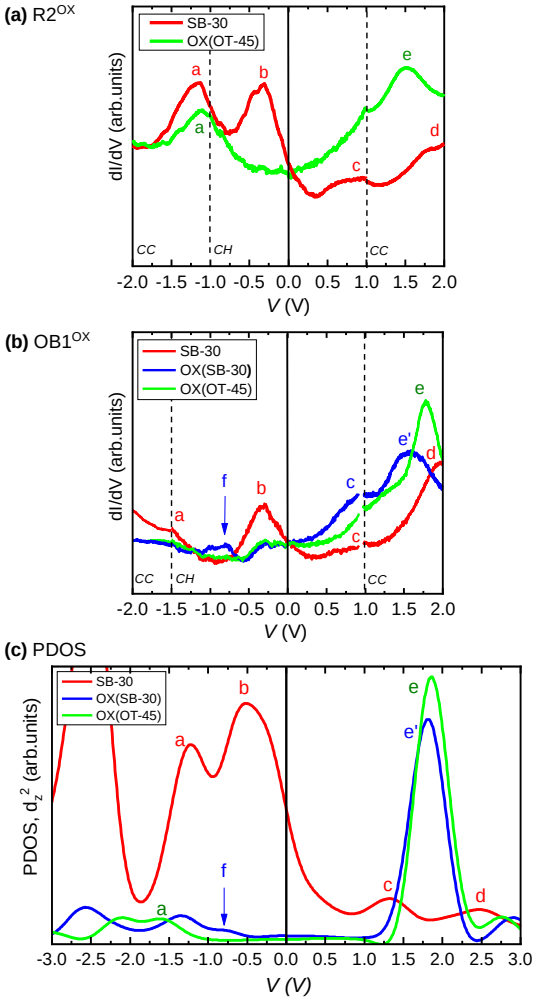

Figure 4. STS spectra at the center of the molecule in the oxidized (a) $R2^{OX}$ phase and (b) $OB1^{OX}$ phase (dotted lines mark the regions measured in either CH or CC modes); (c) DFT-simulated PDOS d_{z^2} component for the SB-30, OX(SB-30) and OX(OT-45) molecular species (see also Fig. S3).

3.3 Probing oxidation of a high-density phase using XLPA.

XLPA measurements at the N K-edge were first performed to reassess the planar arrangement of the FePc molecules on the studied samples. In each of the samples, the vertical (V) and horizontal (H) N K-edge spectra in grazing incidence (γ=70º) were clearly different, exhibiting the characteristic peaks corresponding to π^* and σ^* resonances which allows us to confirm the planar adsorption of the FePc molecules at the Ag(110) surface[29] once placed in the XAS sample holder.

Fig. 5a displays the XLPA at the Fe L_3 edge for the freshly deposited highest density phase OB2. At normal incidence (γ=0º), V and H spectra are coincident (as expected), while in grazing incidence (γ=70º), the linear absorption is strongly dichroic. In particular, the intense peak B in the H configuration is practically quenched in the V one. This behavior was previously observed in R1 and R2 phases, where the B peak was identified with the excitation of the Fe $2p_{3/2}$ electrons to the empty antibonding d_z^2(up) state hybridized with the N-s and N-p_{xy} states of the next neighbor nitrogen atoms[18]. Features A-E, which were also found in R1 and R2, are less pronounced in the OB2 phase.

Fig. 5b shows the evolution of the H-V XLPA spectra obtained in grazing incidence (γ=70º) for four different stages in an oxidation-annealing cycle: OB2→OX1→OX2→ANN, where the O_2 dosing of oxidized samples are given in Table S.1. The evolution observed in the XLPA spectra reflects the evolution of the oxidation reaction, i.e. $OB2^{OX1}$ sample was less oxidized than $OB2^{OX2}$: as the OB2 phase gets oxidized, peak B fades while an intense peak D emerges. The reverse process occurs upon annealing, although the initial state was not completely recovered. The strong structural disorder observed in OB2 upon oxidation by STM (see Fig. 3i) probably justifies the incomplete recover of the pristine sample after annealing.

Qualitatively, a similar behavior was observed upon oxidation of the R2 phase[18], although in that case the D peak was more pronounced, and the process was completely reversible after annealing. In the R2 phase, the FePc molecules have, in principle, space enough to change from SB-30 to OT-45 and back upon oxidation and annealing respectively without much steric hindrance (although collisions between molecules shifted in opposite directions may occur). We associate the intensity transfer from peak B to D upon oxidation with a ~2 eV peak shift, compatible with an increase in the hole density above the Fermi Energy, E_F, which is compatible with the LDOS changes observed in STS on the Fe sites (cf. Fig. 4). It is feasible that that the formation of the FePc-(η^2-O_2)-Ag complex has associated a charge transfer from Fe towards oxygen, increasing the hole density.

Fig. 5c shows the H polarization XLPA spectrum of the oxidized sample $OB2^{OX2}$ (black thick line). The experimental spectrum can be qualitatively approximated by a weighted sum of the spectra obtained for the pristine sample, where non-oxidized FePc molecules are on SB-30 positions (green line), and that of a fully oxidized $R2^{OX}$ sample made of 100% oxidized, rotated OX(OT-45) molecules[18]. By this procedure, we could estimate a yield of 20% of oxidized molecules for $OB2^{OX1}$ and 50% in $OB2^{OX2}$. We conclude that the oxidation of the denser phase OB2 is less effective than for the low-density R2 (comparing these results with those reported in ref. [18] for similar O_2 dosing level, see Fig. 10a). We note that we could reach up to 80% of oxidized species when the sample was exposed in a different chamber to a higher oxygen dosing, as shown by the STM image in Fig. 3i.

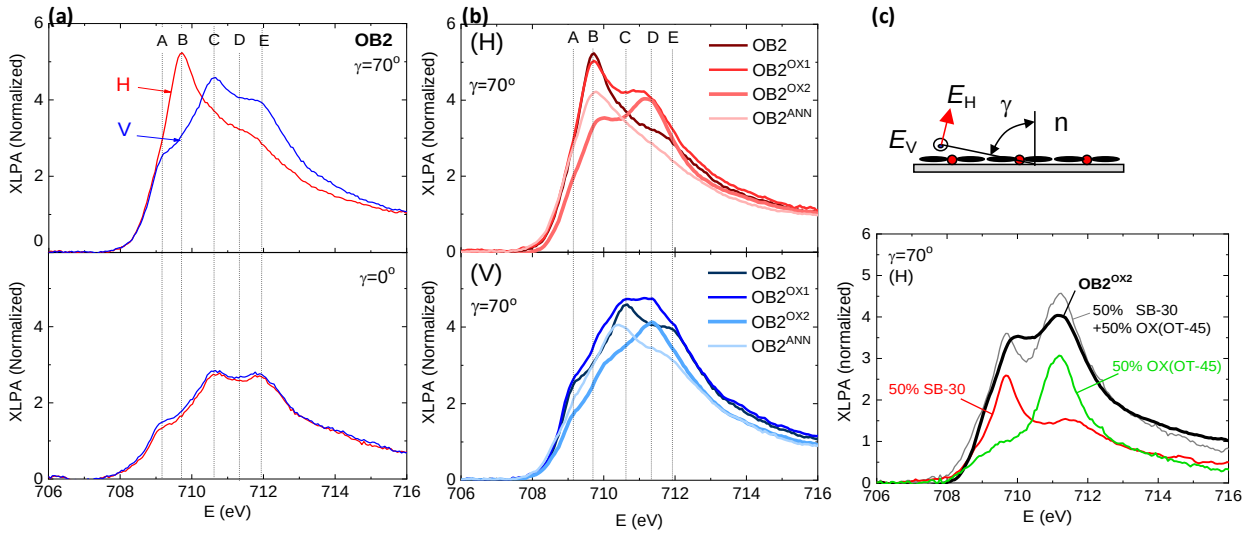

Figure 5. Normalized XLPA of phase OB2 at the Fe L_3 edge before and after oxidation. (a) Non-oxidized grazing incidence (γ=70º) and normal incidence (γ=0º) spectra of two light polarizations; (b) Normalized XLPA in grazing incidence (γ=70º), H and V polarizations, of as deposited phase OB2, oxidized phases $OB2^{OX1}$ and $OB2^{OX2}$ and annealed $OB2^{ANN}$; (c) The normalized XLPA (H polarization) in grazing incidence (γ=70º) of the oxidized phase $R3^{OX2}$ is well predicted by a linear combination of 50% the XLPA of the pristine phase OB2 (containing FePc on SB-30 positions) and 50% the spectrum of the fully oxidized $R2^{ox}$ phase, where all molecules are OX(OT-45). Top inset: schematic view of sample FePc deposited on a Ag substrate. The incoming beam at grazing incidence is shown with the $\vec{E}$ in the *H* and *V* polarization modes.

3.4 Magnetic properties of oxidized high-density phases.

The XAS and XMCD spectra were measured on OB2 and OB1 pristine and oxidized samples at the Fe $L_{2,3}$ edges, under different incident angles from normal to grazing incidence, including the so called "magic angle" to allow the separate determination of Fe spin magnetic moment.

Fig. 6 shows the XAS & XMCD spectra obtained for pristine and oxidized OB2 and OB1 phases (upper and lower panels respectively). First, it has to be noted that Fe in the oxidized FePc-(η^2-O_2)-Ag(110) complex presents a much larger XMCD signal than the pristine FePc-Ag(110), in agreement with the experimental results in R1 and R2 phases[18]. For example, O_2 dosing produces an increase in the XMCD signal in OB1 phase of a factor ~7 at γ=55º. Determination of the fraction of oxidized molecules on each sample and sum rule analysis allows us to properly quantify the orbital and spin magnetic moment of each configuration. Second, it is interesting to remark that although pristine OB2 and OB1 XMCD spectra are essentially equal, and very similar to the XMCD of the R1 and R2 samples, the lineshape of XMCD spectra in the oxidized $OB1^{OX}$ phase is clearly different to that observed in samples $R1^{OX}$, $R2^{OX}$ (Fig. S.7) and $OB2^{OX}$ (Figs. S5 and 6): the intensity of the peak at E=710 eV is uniquely strong in comparison with all the other samples, which is indicative of the presence of a fraction of Fe species with a different electronic structure. This observation correlates with the spectral differences obtained in STS of the different oxidized species previously discussed.

Fig. 7 (left) compares the XMCD spectra along the cycle OB2→OX1→OX2→ANN obtained at γ=0º and γ=70º. The XMCD of pristine FePc on Ag(110) has a $L_{2,3}$ lineshape very similar to that of metallic Fe, suggesting the strong hybridization of Fe in FePc with the metal substrate. Similar results were obtained for other investigated incidence angles (see Fig. S5). The analysis of the spectra evidences an evolution from the as-deposited phase to the most oxidized configuration. The XMCD obtained at the $OB2^{OX1}$ and $OB2^{OX2}$ phases present a progressively larger intensity and a shape evolving towards that observed for non-metallic Fe(III) in a crystal field. After the annealing process, the XMCD recovers the metallic aspect, although the line shape is not exactly coincident with that of the as-deposited sample. Qualitatively, the same behavior was observed along the oxidation-reduction reaction of the R1 and R2 phases[18].

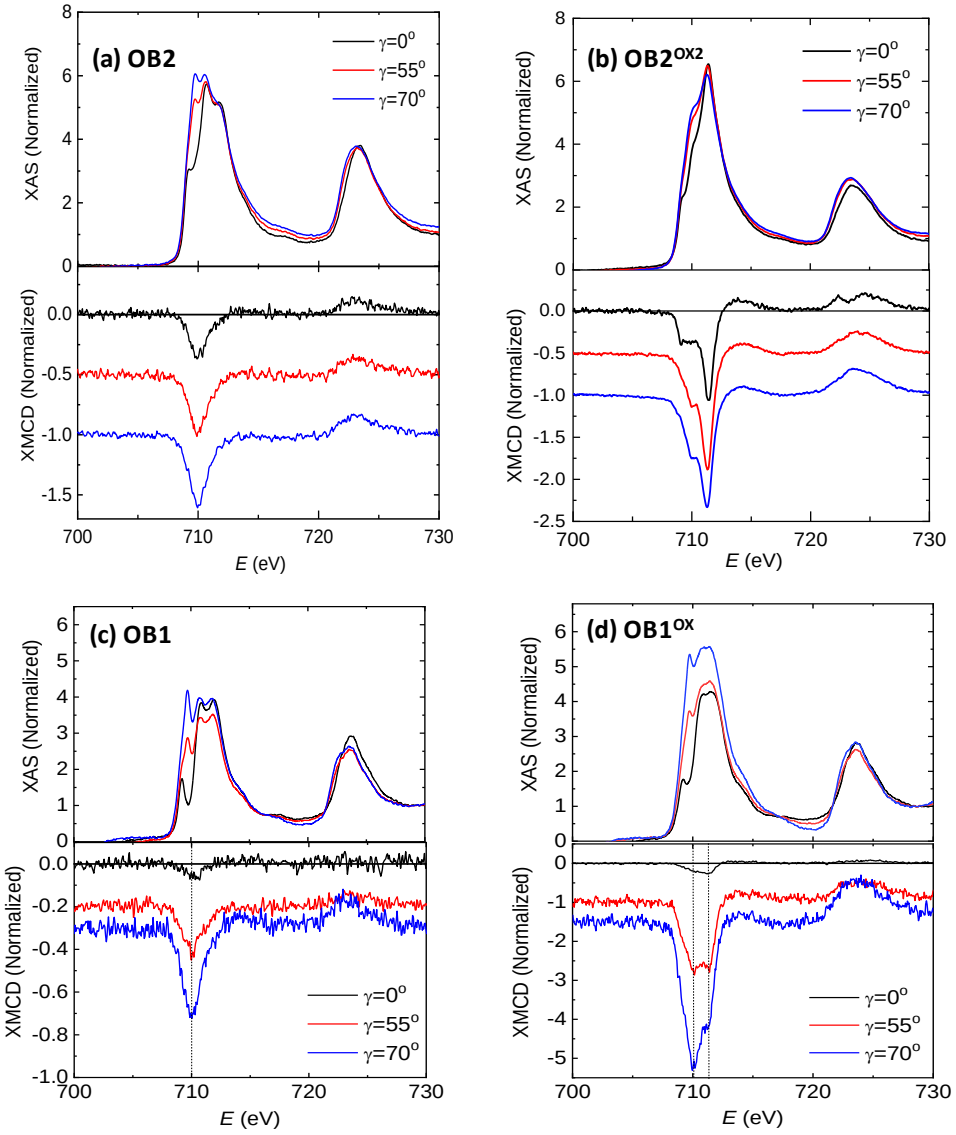

Figure 6. Normalized XAS & XMCD spectra at the Fe $L_{2,3}$ edge measured at different beam incident angles γ, for the (a) pristine R3 and (b) oxygenated $OB2^{OX2}$ samples, at B=6 T, T=5.0 K, and (c) pristine OB1 and (d) oxygenated $OB1^{OX}$ samples, at B=4 T, T=2.8 K.

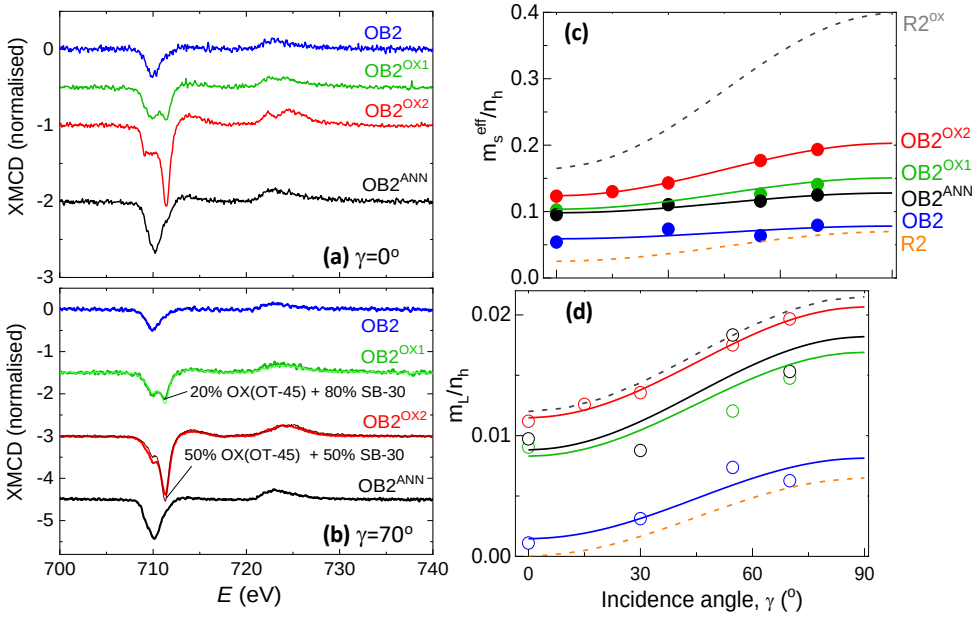

Figure 7. Left: Normalized XMCD spectra of the OB2, OB2^{OX1}, OB2^{OX2}, OB2^{ANN} samples at the Fe $L_{2,3}$ edge, measured at B=6 T, T=5.0 K at an incident angle (a) γ=0º, (b) γ=70º. The thin lines in (b) correspond to the XMCD calculated as the linear combination with (%OX-ROT) percentage of the fully-oxidized LD^{OX} and (%NON-ROT) of the as-evaporated phase; Right: Effective spin moment (c) and orbital moments (per hole) (d) as determined with the sum rules for OB2, OB2^{OX1}, OB2^{OX2} and OB2^{ANN}. The lines in (c) and (d) show the fits using Eqs. [1] and [2], as well as curves earlier reported for low-density phases R2 and R2^{OX}, ref. [16].

The sum rules allow us to determine the orbital and effective spin magnetic moment per hole in the 3d band as a function of the incident angle. The right side of Fig. 7 yields the angular dependence of the orbital and effective spin magnetic moments per 3d hole, m_s^{eff}/n_h and $m_L/n_h(\gamma)$, determined for the OB2, OB2^{OX1}, OB2^{OX2} and OB2^{ANN} phases. For the sake of comparison, the previously determined dependencies for pristine and oxidized low-density R2 phases are also shown.

At a given angle of incidence, the orbital moment per hole can be expressed as a function of its components in the direction perpendicular (m_L^z) and parallel (m_L^{xy}) to the FePc molecular plane as:

$$m_L(\gamma)/n_h = m_L^{xy}/n_h \cdot \sin^2\gamma + m_L^z/n_h \cdot \cos^2\gamma. \qquad [1]$$

On the other hand, the effective spin moment is $m_s^{eff}(\gamma)/n_h = m_s(\gamma)/n_h - 7m_T(\gamma)/n_h$, where m_S is the isotropic spin moment and m_T the angle-dependent intra-atomic spin dipole moment, which is non-negligible in this case. m_T expresses the inhomogeneous spatial distribution of the spin density over the atomic unit cell, due to the anisotropic charge distribution arising from strongly directional bonds or crystal field. In the C_4 symmetry of the FePc molecule, the in-plane (m_T^{xy}) and out-of-plane (m_T^z) components of the dipolar-moment are related by $m_T^z + 2m_T^{xy} = 0$; thus, the effective moment angular dependence $m_s^{eff}(\gamma)/n_h$ can be written as:

$$m_s^{eff}(\gamma)/n_h = m_s/n_h - 7m_T^z/n_h(\cos^2\gamma - \sin^2\gamma/2). \qquad [2]$$

At the magic angle (γ*=54.7º), the dipolar term cancels, and so m_s^{eff} provides directly m_s [30].

The sum rules were applied to obtain the angular dependencies $m_s^{eff}(\gamma)/n_h$ and $m_L(\gamma)/n_h$ (see Fig. 7c and Fig. S6) and the fitting of the experimental data using Eqs. [1] and [2] allowed us to determine m_s/n_h, m_L^z/n_h, m_L^{xy}/n_h and m_T^z/n_h for Fe in pristine, oxidized and annealed OB2 and OB1 samples, which are summarized in Table 1.

All phases display planar anisotropy, in agreement with the previous findings for FePc in diverse environments. However, the highly unquenched orbital magnetic moment of FePc when the molecule is not in contact with a metallic surface ($m_L/m_S \approx 1$)[29,31] is fully lost in FePc/Ag(110) phases, both in the pristine (or annealed) phases as in the oxidized ones.

	m_L^z/n_h	m_L^{xy}/n_h	m_s/n_h	m_T^z/n_h	Ref.
R2	0	6.5x10^{-3}	7.1x10^{-2}	4.3x10^{-3}	[18]
R2D^{OX}	1.2x10^{-2}	2.2x10^{-2}	3.7x10^{-1}	2.9x10^{-2}	[18]
R2^{ANN}	4.0x10^{-3}	1.5x10^{-2}	7.1x10^{-2}	5.9x10^{-3}	[18]
OB2	1.4x10^{-3}	8.1x10^{-3}	7.2x10^{-2}	1.8x10^{-3}	*
OB2^{OX1}	8.3x10^{-3}	1.7x10^{-2}	1.3x10^{-1}	4.5x10^{-3}	*
OB2^{OX2}	1.1x10^{-2}	2.1x10^{-2}	1.8x10^{-1}	7.5x10^{-3}	*
OB2^{ANN}	8.8x10^{-3}	1.8x10^{-2}	1.2x10^{-1}	2.8x10^{-3}	*
OB1	1.5x10^{-3}	1.2x10^{-2}	5.2x10^{-2}	5.6x10^{-3}	*
OB1^{OX}	2.0x10^{-3}	4.2x10^{-2}	4.9x10^{-1}	6.2x10^{-2}	*

Table 1. Magnetic moment parameters (in units of μ_B/hole) for the different FePc/Ag(110) samples. * This work.

3.5 Discussion

Fig. 8 shows a comparison of the XMCD at γ=55º of the two oxidized high density phases $OB2^{OX2}$ and $OB1^{OX}$. Oxygen exposure produces in both cases an increase in the dichroic signal compared to the pristine cases; however, differences in the spectra are observed, which should be correlated with the different molecular species detected by STM.

The XMCD of the oxidized $OB2^{OX}$ phases can be well fitted using a linear combination of the experimental signals obtained from the pristine OB2 sample and the fully oxidized sample, i.e. a linear combination of non-oxidized FePc on SB-30 and oxidized OX(OT-45) molecules, as shown in Fig. 8a. For the $OB2^{OX1}$ and $OB2^{OX2}$ samples the percentages of pristine vs. oxidized molecules are 50-50 and 80-20, respectively, matching the values found for the XLPA fitting (Fig. 5c).

Qualitatively, the XMCD of the $OB2^{OX}$ oxidized phases resemble that of the previously reported rectangular $R2^{OX}$ oxidized phase, which contained a major fraction of oxidized OX(OT-45) molecules and some pristine molecules occupying SB-30 sites. It is interesting to note that the spectrum of the OX(OT-45) molecules very closely corresponds to Fe^{3+} oxidation state in an octahedral site, as previously shown by Ligand Field Multiplet (LFM) calculations[18] (Fig. S7).

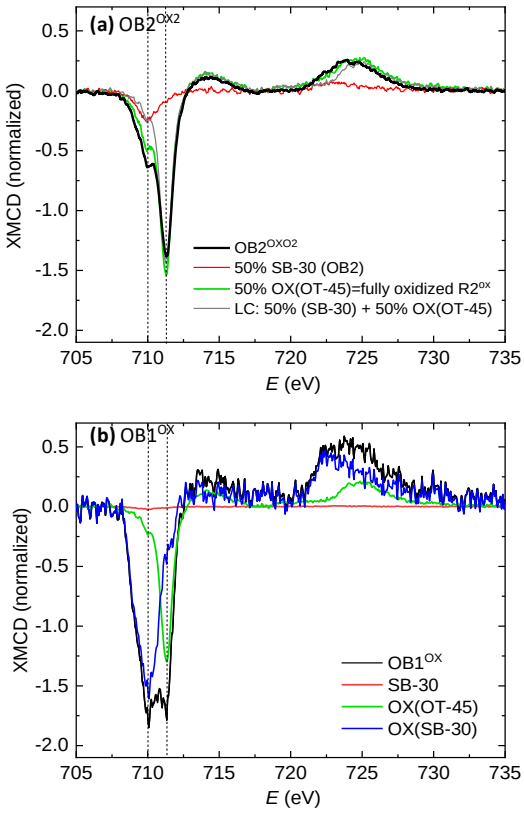

Figure 8. Comparison of XMCD (γ=55º) of oxidized phases: (a) $OB2^{OX2}$ (*B*=6 T, *T*=3.4 K): the measured spectrum can be expressed as a linear combination of the spectra of non-oxidized SB-30 molecules, and oxidized, rotated OX(OT-45) molecules; (b) $OB2^{OX}$ (*B*=4 T, *T*=6.0 K): the measured spectrum is a linear combination of the spectra of three molecule species: SB-30, OX(OT-45) and OX(SB-30).

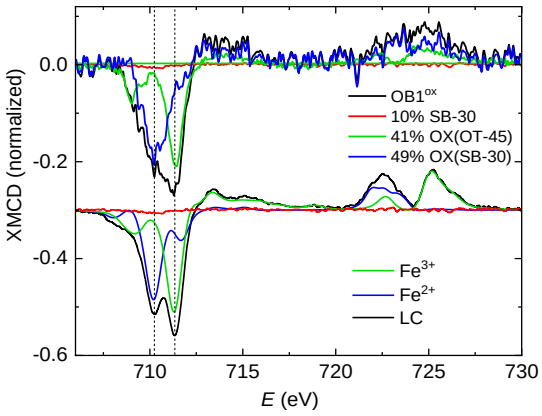

Figure 9. Above: XMCD of $OB1^{OX}$ phase (*T*=5.0 K, *B*=6 T, γ=0º): it can be described as a linear combination of the spectra of the SB-30, OX(OT-45) and OX(OT-30) molecules; below (vertically shifted for comparison), spectra of Fe^{3+} and Fe^{2+} simulated with CTM4XAS 5.0 program[32] including spin-orbit coupling, crystal field (CF) effects and reduction of the Slater integrals to include the interatomic configuration interaction. The parameters used for the simulations were close to those of ref.[12]: the CF parameters were $10D_q$=1.86 eV, 1.0 eV (D_t=D_s=0) for Fe^{3+}Oh, Fe^{2+}Oh (Oh: octahedral site) respectively; a Slater reduction of 70%, 80%, 75% was used to F(dd), F(pd) and G(pd). The results were convoluted by a Lorentzian of Γ=0.3(0.4) eV for the $L_3(L_2)$ edge to account for intrinsic core-hole lifetime broadening, and by a Gaussian of σ=0.2 eV to account for instrumental broadening.

In contrast, the XMCD of the $OB1^{OX}$ oxidized sample cannot be described considering only these two species. In view of the STM images obtained in this sample (Fig. 3h), we require an additional component for the OX(SB-30) molecules that in the XMCD accounts for the dichroic signal contribution observed at 710.6 eV.

This contribution can be empirically determined, as shown in Fig. 8b: to obtain the XMCD of the oxidized OX(OT-30) molecules (blue line), we subtract from the experimental XMCD of the

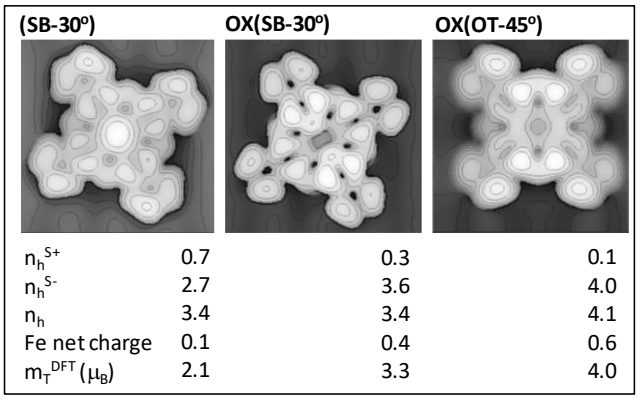

Table 2. DFT simulations of STM images in CC mode at *V*=1 V (top), and (bottom) the Fe 3d S^+ holes (n_h^{S+}) and S^- holes (n_h^{S-}), the Fe net charge, the number of holes (n_h $n_h = n_h^{S+} + n_h^{S-}$) and the magnetic moment (m_{TOT}^{DFT}), for the non-oxidized (left), oxidized-rotated (center) and oxidized non-rotated (right) species.

Phase	FePc	$m_L^{xy}(\mu_B)$	$m_s(\mu_B)$	$m_{TOT}(\mu_B)$	Factor
$R2^{OX}$	SB-30	$2.2x10^{-2}$	0.241	0.26	
	OX(OT-45)	$1.1x10^{-1}$	2.062	2.17	8.3
$R3^{OX}$	SB-30	$2.7x10^{-2}$	0.244	0.27	
	OX(OT-45)	$2.1x10^{-1}$	1.59	1.80	6.7
OB^{OX}	SB-30	$4.1x10^{-2}$	0.178	0.22	
	OX(OT-45)	$1.1x10^{-1}$	2.062	2.17	9.9
	OX(SB-30)	$3.6x10^{-1}$	1.87	2.23	10.1

Table 3. Magnetic moments determined for the different types of molecules found in the oxidized FePc/Ag(110) phases.

oxidized sample $OB1^{OX}$ a weighted sum of the XMCD from non-oxidized (SB-30) molecules (red line) and from oxidized OX(OT-45) molecules (green line), see S9 for details. The residue XMCD peak at the energy of 710.6 eV in the spectrum of oxidized unrotated molecules, OX(SB-30), is quite different from the energy of the main peak (711.3 eV) obtained for the spectrum of rotated molecules, OX(OT-45). This suggests different Fe oxidation states in these two species.

In order to test this hypothesis, we calculated the XMCD spectra of Fe^{3+} and Fe^{2+} spectra within a LFM model using CTM4XAS 5.0[32] . This version of the program allows only to simulate the XMCD spectra in normal incidence conditions. The results of our calculations are shown in Fig. 9: a linear combination of the pristine OB1 (weighed by 10%) plus the calculated Fe^{2+} and Fe^{3+} spectra (with weights of 49% and 41%, respectively) nicely describe the experimental XMCD (at $\gamma=0^o$) of the $OB1^{OX}$ phase. This calculation strongly supports our assignment of the oxidized FePc at OX(OT-45) as Fe^{3+} and OX(SB-30) as Fe^{2+}, justifying the local spectroscopic difference of the two species and showing the strength of the combination of STM, STS and XMCD techniques.

To complete our study, we performed DFT calculations on the three different types of FePc species relevant for our work, namely, the pristine FePc on SB-30 positions, and oxidized molecules OX(OT-45) and OX(SB-30). The calculation yields the local density of states, allowing to obtain the 3d spin-polarized number of holes n_h , the Fe net charge, and the magnetic moment for each species, as reported in Table 2.

In agreement with our XMCD and STS experimental results, DFT calculations show that oxidized unrotated OX(SB-30) molecules have a smaller Fe net charge (0.4 e^-) than the rotated OX(OT-45), with (0.6 e^-).

We used the values in Table 1 together with the number of holes in the 3d band from DFT to obtain absolute values for the magnetic moments of the different molecular species. The results are listed in Table 3. Upon oxidation, the total moment increases from m_T=0.27 μ_B to 1.2-1.6 μ_B in the OB2 phase, which is a factor ≈6.5, and from m_T=0.18 μ_B to 2.2 μ_B in the OB1 phase, which is a factor ≈10, for both species, i.e. OX(OT-45) and OX(SB-30). We note that DFT-calculated total magnetic moment values are larger than the experimental ones, as previously reported[18]. Notably, although steric hindrance makes the accommodation of O_2 in dense phases more difficult, we find that the increase in the magnetic moment of the oxidized FePc molecules is of the same order as in the low-density phases (see Table 3).

In conclusion, Figure 10 summarizes the oxygenation and magnetic moment capabilities found for the three studied FePc/Ag(110) phases upon O_2 dosing. As shown in Fig. 10a, the percentage of oxidized molecules in the sample can be controlled by O_2 dosing. The oxygenation process is most efficient in the low-density R1/R2 phases, followed by the high-density R3/OB2 phases, and is more difficult in the more distorted OB1 phase. Interestingly, by virtue of the upturn in the magnetic moment produced in the oxidized FePc species, the average magnetic

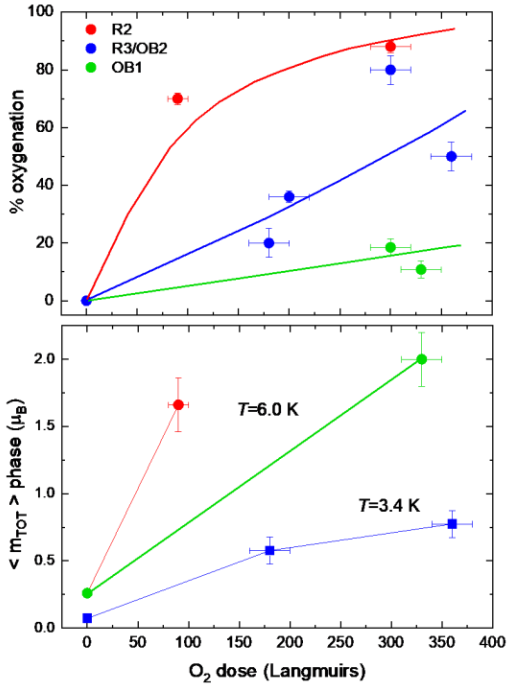

Figure 10. (a) Percentage of oxygenated molecules, and (b) average magnetic moment per Fe atom in a ML sample, as a function of the oxygen dose, for the three studied phases: the low-density R2 and high-density R3/OB2 and OB1 phases. Lines are guides for the eye.

moment of the oxidized samples ($< m_{TOT} >$ per Fe atom) can be tuned between ~ 0.2-2 μ_B by controlling the O_2 dose (see Fig. 10b). Conversely, this property might be potentially tailored to device a magnetic oxygen sensor.

4. CONCLUSIONS

In this work we have investigated the oxygen-induced magnetic moment changes of FePc molecules of high-density sub-ML and ML phases on the Ag(110) substrate. The oxidation rate of the dense, quasi-squared R3/OB2 phases is comparable to the previously reported rectangular low-density (R1 and R2) phases. Owing to steric impediments, the oblique phase (OB1) is less effective in the oxidation-reduction reaction.

In the R3/OB2 phases, the oxidation takes place accompanied by a lateral shift of the molecule, which moves the Fe centre from SB to OT position, accompanied by a rotation of ≈15º, giving rise to the FePc-(η^2-O_2)-Ag complex. This is accompanied by an increase by a factor ~6.5 of the Fe total magnetic moment. Upon annealing, the magnetic moment decreases to a value close to that for the non-oxidized phase. However, full reversibility (as found in R1 and R2 phases) is prevented by the large disorder induced by oxidation.

For the OB1 phase, oxygen diffusion becomes even more difficult. In order to accommodate O_2, a fraction of molecules do rotate and move to OT-45 sites, while the rest is able to accommodate oxygen while keeping their initial SB-30 positions, due to the highly restricted molecular movement.

The oxidation mode leading to the two different types of oxidized FePc species affects markedly the electronic density of states, as proven by our STS and XMCD experiments, and DFT and Ligand Field Multiplet calculations: the XMCD spectrum corresponding to the oxidized unrotated OX(SB-30) molecule

shows a characteristic of the Fe^{2+} oxidation state, while that of rotated OX(OT-45) is reminiscent to that of Fe^{3+}. The Fe magnetic moment remains in all cases with planar anisotropy. Interestingly, both oxidized species show an increased magnetic moment by a factor ~10.

Even though the molecular density of the R3/OB2 phases is larger than that of the OB1 phase, we find that the oxidation of R3/OB2 is easier, and the species of oxidized FePc resemble those found in the rectangular phases. Thus, the unit cell configuration of the ML assembly determines their oxygen capture properties.

Our systematic study shows that despite the steric limitations FePc molecules in high-density FePc/Ag(110) phases are able to intercalate oxygen through different mechanisms. Therefore, control of the magnetic moment of the system in a range between 0.2 to 2.2 μ_B can be easily exerted through oxygen dosing.

ASSOCIATED CONTENT

S1. Structural transition from R3 to OB2 phases; S2. Oxygen dosages; S3. Zoology of molecules in oxidized high-density phases; S4. DFT PDOS calculations; S5. Phase R3, N K-edge; S6. Angular XAS & XMCD spectra for $OB2^{OX1}$ and $OB2^{ANN}$; S7. Angular dependence of magnetic moments for OB1; S8. $R2^{OX}$ XMCD and Ligand Field Multiplet (LFM) calculations; S9. Percentages of molecular species in OB^{OX} oxidized phase.

AUTHOR INFORMATION

Corresponding Author
*Phone: +34 932805524.
E-mail: ebartolome@euss.es

ACKNOWLEDGEMENTS

We acknowledge financial support from the DWARFs project MAT2017-83468-R and from the European Regional Development Fund (ERDF) under the program Interreg V-A España-Francia-Andorra (Contract No. EFA 194/16 TNSI). M.P. and A.M. are funded by the CERCA Program/ Generalitat de Catalunya, and the Severo Ochoa program from Spanish MINECO (Grant No. SEV-2017-0706). The XMCD experiments were performed at the BOREAS beamline of the ALBA Synchrotron Light Facility (Barcelona, Spain) and at the ID32 beamline at the European Synchrotron Radiation Facility-ESRF (Grenoble, France). We are grateful to the beamline staff for providing assistance in using both beamlines.

REFERENCES

(1) Anand, M.; Siahrostami, S.; Norskov, J. K. Exploring the Effect of Gold Support on the Oxygen Reduction Reaction Activity of Metal Porphycenes. *Chem.Cat.Chem.* **2018**, *23*, 5505–5510.

(2) Bartolome, F.; Bunau, O.; Garcia, L. M.; Natoli, C. R.; Piantek, M.; Pascual, J. I.; Schuller, I. K.; Gredig, T.; Wilhelm, F.; Rogalev, A.; et al. Molecular Tilting and Columnar Stacking of Fe Phthalocyanine Thin Films on Au(111). *J. Appl. Phys.* **2015**, *117* (17), 17A735.

(3) Stepanow, S.; Miedema, P. S.; Mugarza, A.; Ceballos, G.; Moras, P.; Cezar, J. C.; Carbone, C.; De Groot, F. M. F.; Gambardella, P. Mixed-Valence Behavior and Strong Correlation Effects of Metal Phthalocyanines Adsorbed on Metals. *Phys. Rev. B - Condens. Matter Mater. Phys.* **2011**. https://doi.org/10.1103/PhysRevB.83.220401.

(4) Molodtsova, O. V; Knupfer, M.; Ossipyan, Y. A.; Aristov, V. Y. Molecular Orientation and Ordering in CoPc and FePc Thin Films Grown on Au(001)-5 X 20. *J. Appl. Phys.* **2008**, *104* (8), 083704.

(5) Mugarza, A.; Robles, R.; Krull, C.; Korytár, R.; Lorente, N.; Gambardella, P. Electronic and Magnetic Properties of Molecule-Metal Interfaces: Transition-Metal Phthalocyanines Adsorbed on Ag(100). *Phys. Rev. B - Condens. Matter Mater. Phys.* **2012**, *85*, 155437. https://doi.org/10.1103/PhysRevB.85.155437.

(6) Palmgren, P.; Yu, S.; Hennies, F.; Nilson, K.; Åkermark, B.; Göthelid, M. Changing Adsorption Mode of FePc on TiO2(110) by Surface Modification with Bipyridine. *J. Chem. Phys.* **2008**, *129* (7), 074707.

(7) Åhlund, J.; Nilson, K.; Palmgren, P.; Göthelid, E.; Schiessling, J.; Göthelid, M.; Mårtensson, N.; Puglia, C. Molecular Growth Determined by Surface Domain Patterns. *J. Phys. Chem. C* **2008**, *112* (17), 6887–6890.

(8) Hu, F.; Mao, H.; Zhang, H.; Wu, K.; Cai, Y.; He, P. Electronic and Structural Properties at the Interface between Iron-Phthalocyanine and Cu(110). *J. Chem. Phys.* **2014**, *140*, 094704.

(9) Scarfato, A.; Chang, S. H.; Kuck, S.; Brede, J.; Hoffmann, G.; Wiesendanger, R. Scanning Tunneling Microscope Study of Iron(II) Phthalocyanine Growth on Metals and Insulating Surfaces. *Surf. Sci.* **2008**, *602* (3), 677–683.

(10) Ohta, N.; Arafune, R.; Tsukahara, N.; Takagi, N.; Kawai, M. Adsorbed States of Iron(II) Phthalocyanine on Ag(111) Studied by High-Resolution Electron Energy Loss Spectroscopy. In *Surf.&Interf.Anal.*; 2014; pp 1253–1256.

(11) Takami, T.; Carrizales, C.; Hipps, K. W. Commensurate Ordering of Iron Phthalocyanine on Ag(111) Surface. *Surf. Sci.* **2009**, *603* (21), 3201–3204.

(12) Åhlund, J.; Schnadt, J.; Nilson, K.; Göthelid, E.; Schiessling, J.; Besenbacher, F.; Mårtensson, N.; Puglia, C. The Adsorption of Iron Phthalocyanine on Graphite: A Scanning Tunnelling Microscopy Study. *Surf. Sci.* **2007**, *601* (17), 3661–3667.

(13) Dou, W.; Yang, Q.; Lee, C.-S. Anisotropic Film Growth of Iron-Phthalocyanine on Graphene on a Ni(111) Substrate: Roles of Molecule-Substrate and Intermolecular Interaction. *Appl. Phys. Lett.* **2013**, *102*, 131606.

(14) Palmgren, P.; Angot, T.; Nlebedim, C. I.; Layet, J. M.; Le Lay, G.; Göthelid, M. Ordered Phthalocyanine Superstructures on Ag(110). *J. Chem. Phys.* **2008**, *128* (6).

(15) Casarin, M.; Di Marino, M.; Forrer, D.; Sambi, M.; Sedona, F.; Tondello, E.; Vittadini, A.; Barone, V.; Pavone, M. Coverage-Dependent Architectures of Iron Phthalocyanine on Ag(110): A Comprehensive STM/DFT Study. *J. Phys. Chem. C* **2010**, *114* (5), 2144–2153.

(16) Sedona, F.; Di Marino, M.; Forrer, D.; Vittadini, A.; Casarin, M.; Cossaro, A.; Floreano, L.; Verdini, A.; Sambi, M. Tuning the Catalytic Activity of Ag(110)-Supported Fe Phthalocyanine in the Oxygen Reduction Reaction. *Nat. Mater.* **2012**, *11* (11), 970–977.

(17) Cai, Y. .; Rehman, R. A.; Ke, W.; Zhang, H.-J.; He, P.; Bao, S. The Transition Behavior of FePc on Ag(110). *Chem. Phys. Lett.* **2013**, *582*, 90–94.

(18) Bartolomé, J.; Bartolomé, F.; Brookes, N. B.; Sedona, F.; Basagni, A.; Forrer, D.; Sambi, M. Reversible Fe Magnetic Moment Switching in Catalytic Oxygen Reduction Reaction of Fe-Phthalocyanine Adsorbed on Ag(110). *J. Phys. Chem. C* **2015**, *119* (22), 12488–12495.

(19) Sedona, F.; Lo Cicero, M.; Carlotto, S.; Basagni, A.; Fakhrabadi; Fakhrabadi, M. M. S.; Casarin, M.; Sambi, M. Substrate Involvement in Dioxygen Bond Dissociation Catalysed by Iron Phthalocyanine Supported on Ag(100).

Chem. Commun. **2018**, *54* (6).

(20) Jones, E. .; Rocha, T. C. R.; Knop-Gericke, A.; Stampfl, C.; Schlöglb, R.; Piccinina, S. Jones. *Phys.Chem.Chem.Phys* **2015**, *17*, 9288.

(21) Giannozzi, P.; Baroni, S.; Bonini, N.; Calandra, M.; Car, R.; Cavazzoni, C.; Ceresoli, D.; Chiarotti, G. L.; Cococcioni, M.; Dabo I., et al. QUANTUM ESPRESSO: A Modular and Open-Source Software Project for Quantum Simulations of Materials. *J. Phys. Condens. Matter* **2009**, *21*, 395502–395520.

(22) Perdew, J. P.; Burke, K.; Ernzerhof, M. Generalized Gradient Approximation Made Simple. *Phys. Rev. Lett.* **1996**, *77*, 3865–3868.

(23) Vanderbilt, D. Soft Self-Consistent Pseudopotentials in a Generalized Eigenvalue Formalism. *Phys. Rev. B* **1990**, *41*, 7892−7895.

(24) Scherlis, D. A.; Cococcioni, M.; Sit, P.; Marzari, N. Simulation of Heme Using DFT + U: A Step toward Accurate Spin-State Energetics. *J. Phys. Chem. B* **2007**, *111*, 7384−7391.

(25) Tersoff, J.; Hamann, D. R. Theory and Application for the Scanning Tunneling Microscope. *Phys. Rev. Lett.* **1983**, *50*, 1998.

(26) Barla, A. A.; Nicolás, J.; Cocco, D.; Valvidares, S. M.; Herrero-Martín, J.; Gargiani, P.; Moldes, J.; Ruget, C.; Pellegrin, E.; Ferrer, S. Design and Performance of BOREAS, the Beamline for Resonant X-Ray Absorption and Scattering Experiments at the ALBA Synchrotron Light Source. *J. Synchrotron Rad.* **2016**, *23*, 1507–1517.

(27) Kummer, K.; Fondacaro, A.; Jimenez, E.; Velez-Fort, E.; Amorese, A.; Aspbury, M.; Yakhou-Harris, F.; van der Linden, P.; Brookes, N. B. The High-Field Magnet Endstation for X-Ray Magnetic Dichroism Experiments at ESRF Soft X-Ray Beamline ID32. *J. Synchrotron Rad.* **2016**, *23*, 464–473.

(28) Brookes, N. B.; Yakhou-Harris, F.; Kummer, K.; Fondacaro, A.; Cezar, J. C.; Betto, D.; Velez-Fort, E.; Amorese, A.; Ghiringhellib, G.; Braicovicha, L.; et al. The Beamline ID32 at the ESRF for Soft X-Ray High Energy Resolution Resonant Inelastic X-Ray Scattering and Polarisation Dependent X-Ray Absorption Spectroscopy. In *Nuclear Instruments and Methods in Physics Research Section A: Accelerators, Spectrometers, Detectors and Associated Equipment,903, 21*; 2018; pp 175–192.

(29) Bartolomé, J.; Bartolomé, F.; García, L. M.; Filoti, G.; Gredig, T.; Colesniuc, C. N.; Schuller, I. K.; Cezar, J. C. Highly Unquenched Orbital Moment in Textured Fe-Phthalocyanine Thin Films. *Phys. Rev. B - Condens. Matter Mater. Phys.* **2010**, *81* (19), 195405.

(30) Stöhr, J.; König, H. Determination of Spin- and Orbital-Moment Anisotropies in Transition Metals by Angle-Dependent X-Ray Magnetic Circular Dichroism. *Phys. Rev. Lett.* **1995**, *75* (20), 3748–3751.

(31) Bartolomé, J.; Bartolomé, F.; García, L. M.; Gredig, T.; Schuller, I. K.; Cezar, J. C. Magnetic Anisotropy in Fe Phthalocyanine Film Deposited on Si(110) Substrate: Standing Configuration. *Low Temp. Phys.* **2017**, *43* (8), 955–959.

(32) Stavitski, E.; de Groot, F. M. F. The CTM4XAS Program for EELS and XAS Spectral Shape Analysis of Transition Metal L Edges. *Micron* **2010**, *41* (7), 687–694.

TOC image

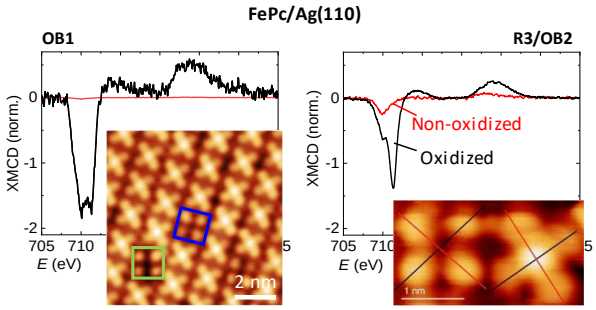
FePc/Ag(110)
OB1
R3/OB2
XMCD (norm.)
0
-1
-2
705
710
E (eV)
2 nm
Non-oxidized
Oxidized
1 nm